



Analysis of Clay Based Cementitious Nanofluid Subjected to Newtonian Heating and Slippage Conditions with Constant Proportional Caputo Derivative



Saqib Murtaza^{1*}, Zubair Ahmad²

¹ Department of Mathematics, King Mongkut's University of Technology, 10140 Bangkok, Thailand

² Dipartimento di Matematica e Fisica, Università degli Studi della Campania “Luigi Vanvitelli”, 81100 Caserta, Italy

* Correspondence: Saqib Murtaza (Saqib.murtaza@mail.kmutt.ac.th)

Received: 03-12-2024

Revised: 04-30-2024

Accepted: 05-08-2024

Citation: S. Murtaza and Z. Ahmad, “Analysis of clay based cementitious nanofluid subjected to Newtonian heating and slippage conditions with constant proportional Caputo derivative,” *GeoStruct. Innov.*, vol. 2, no. 2, pp. 53–67, 2024. <https://doi.org/10.56578/gsi020201>.



© 2024 by the author(s). Published by Acadlore Publishing Services Limited, Hong Kong. This article is available for free download and can be reused and cited, provided that the original published version is credited, under the CC BY 4.0 license.

Abstract: Recent advancements have seen the integration of nanocomposites, composed of clay minerals and polymers, into cementitious materials to enhance their mechanical properties. This investigation focuses on the dynamics of clay-based cementitious nanofluids along a vertical plate, adopting a Jeffrey fluid model to encompass various phenomena. The effects of a first-order chemical reaction and heat generation/absorption are considered, alongside slip velocity and Newtonian heating conditions. The governing equations, represented as partially coupled partial differential equations, have been extended using a constant proportional Caputo (CPC) fractional derivative. Exact solutions were derived employing the Laplace transform technique. A detailed graphical analysis was conducted to elucidate the influence of pertinent flow parameters on the velocity, temperature, and concentration profiles. It was observed that the incorporation of clay nanoparticles results in a reduction of the fluid’s heat transfer rate by 10.17%, and a decrease in the mass transfer rate by 1.31% at a nanoparticle volume fraction of 0.04. These findings underscore the nuanced role of nanoparticle concentration in modifying fluid dynamics under the studied conditions, providing a validated and precise understanding of nanofluid behavior in construction-related applications. This research not only supports the potential of nanotechnology in improving cementitious materials but also contributes to the broader field of fluid mechanics by integrating complex heating and slip conditions into the study of nanoparticle-enhanced fluids.

Keywords: Cementitious fluid; Clay nanoparticles; Newtonian heating; Fractional derivative; Zakian’s algorithm

1 Introduction

Nanomaterials play a significant role in cementitious fluids for a variety of reasons. Firstly, the incorporation of nanoparticles, such as nanosilica or nanoclays, can significantly enhance the mechanical properties of cementitious materials. These nanoparticles act as nucleation sites for the formation of hydration products, resulting in denser microstructures and improved mechanical strength. Moreover, nanomaterials can enhance the durability of cementitious materials by reducing permeability, thereby increasing resistance to chemical attack and improving resistance to freeze-thaw cycles. This is particularly important for infrastructure applications where longevity is crucial. Additionally, nanoparticles can improve the thermal properties of cementitious materials, such as thermal conductivity and heat storage capacity. This is important for applications where thermal insulation or thermal mass is desired, such as in building construction. Furthermore, by improving the mechanical and durability properties of cementitious materials, nanomaterials can contribute to the development of more sustainable construction practices. This can lead to reduced maintenance requirements, a longer service life, and ultimately a lower environmental impact. Lastly, nanomaterials offer the possibility of tailoring the properties of cementitious fluids to meet specific application requirements. By adjusting factors such as particle size, shape, and surface chemistry, engineers can design cementitious materials with desired properties, such as increased strength, improved workability, or enhanced self-healing capabilities. Overall, the incorporation of nanomaterials in cementitious fluids represents a promising avenue for advancing the performance, durability, and sustainability of concrete and other cement-based materials in

various construction and infrastructure applications [1–7]. Keeping in view the importance of the nanomaterials in cementitious fluids, Sheikh et al. [8] examined the flow of Jeffrey fluid containing zinc oxide (ZnO) nanostructures. The flow of Jeffrey fluid containing ZnO nanostructures was modeled using partial fractional differential equations via the Atangana-Baleanu fractional derivative approach and solved using integral transformation. The findings suggest that the addition of 4% ZnO nanoparticles increases skin friction by up to 15%, thereby enhancing the adhesion capacity and strength of concrete, with potential applications in various sectors of construction engineering and management. Murtaza et al. [9] investigated the amalgamated effect of viscous dissipation and joule heating on the electro-osmotic flow of Maxwell nanofluid in a channel. Exact solutions were employed as benchmarks for numerical and empirical approaches. Notably, the incorporation of nanoclay in concrete led to a significant 25.5% enhancement in heat transfer rates, offering potential advancements in concrete-based applications. Khan et al. [10] explored the effects of graphite-aluminum oxide hybrid nanoparticles in water-based fluids with added heat generation in a porous medium, employing momentum and energy equations solved via the Laplace transform method. The findings reveal that the addition of hybrid nanoparticles enhances velocity control and reduces fluid temperature compared to simple nanofluids, with a notable 37.41% increase in heat transfer rate observed with hybrid nanofluids. Further enhancements of up to 11.15% were achieved using different nanoparticle shapes in the base fluid.

Fractional derivatives serve as indispensable tools in fluid dynamics models, particularly when analyzing the intricate behavior of non-Newtonian fluids like cementitious materials. These derivatives offer a refined mathematical framework essential for characterizing the diverse flow phenomena exhibited by such fluids. Unlike their Newtonian counterparts, non-Newtonian fluids display variable viscosity dependent on factors like shear rate, stress, and time, necessitating the utilization of fractional calculus to accurately capture their behavior. In the context of cementitious fluids, fractional derivatives play a pivotal role in modelling complex flow dynamics, including thixotropy, viscoelasticity, and yield stress behaviors. Moreover, they facilitate the modelling of anomalous diffusion phenomena, which is crucial for understanding particle dispersion within the fluid matrix and its impact on properties such as setting time and strength development. Fractional calculus also introduces memory effects into the models, accounting for the history-dependent behavior inherent in many cementitious materials. Additionally, using a multiscale approach, fractional derivatives allow researchers to comprehensively analyze the interplay of different length and time scales, providing deeper insights into the flow properties and behavior of cementitious fluids [11–17].

The preceding literature review highlights a gap in the investigation of the use of the CPC derivative in Jeffrey nanofluid analysis. To address this gap, this study focused on clay-based cementitious Jeffrey nanofluids under conditions involving Newtonian heating, heat generation, and chemical reactions. The conventional classical model was fractionalized using the CPC operator and subsequently solved utilizing the Laplace transform method. The study presents graphical representations of dimensionless parameters and offers scientific insights to enhance comprehension of the phenomena at hand. This study aims to improve the understanding of how cementitious nanocomposites can be enhanced in mechanical strength by incorporating clay minerals and polymers. The Jeffrey fluid model was used to explain complex phenomena such as first-order chemical reactions, heat generation or absorption, slip velocity, and Newtonian heating. This study offers valuable contributions by enhancing the understanding of clay-based nanofluids' effects on cementitious materials. Clay nanoparticles play a critical role in heat and mass transfer rates, making them exceptionally valuable for engineering applications. The knowledge gained from this research allows for the design of advanced cementitious composites with improved thermal and mechanical properties, making them perfect for construction in extreme temperature environments. Moreover, the use of the CPC fractional derivative marks a novel computational approach that improves the modelling of complex fluid behavior. This innovative method could potentially be applied to other nanofluid systems, expanding its utility across various fields.

2 Methodology

The study investigates the dynamics of unsteady, natural convection, and incompressible flow of the Jeffrey nanofluid within a cementitious fluid, taking into account the influence of thermal radiation, heat generation, and Newtonian heating. Clay nanoparticles were uniformly dispersed within the cementitious fluid to create the nanofluid. Flow analysis was conducted with the vertical orientation of a flat plate along the x-axis and perpendicular to the y-axis. A transverse magnetic field, denoted as B_0 , was applied, though the induced magnetic field was deemed negligible and omitted from consideration. Initially, both the fluid and the plate remained static, but they subsequently accelerated with a relative velocity (slip). However, the fluid's temperature increased with the isothermal temperature and concentration level. Figure 1 shows the flow characteristics of the Jeffrey nanofluid.

In light of the assumptions, the velocity governing the equation for the Jeffery nanofluid is as follows:

$$\rho_{nf} \frac{\partial u(\zeta, \tau)}{\partial \tau} = \frac{\mu_{nf}}{1 + \lambda_1} \left(1 + \lambda_2 \frac{\partial}{\partial \tau}\right) \frac{\partial^2 u(\zeta, \tau)}{\partial \zeta^2} + \frac{\mu_{nf} \phi}{K(1 + \lambda_1)} \left(1 + \lambda_2 \frac{\partial}{\partial \tau}\right) u(\zeta, \tau) - \sigma_{nf} B_0^2 u(\zeta, \tau) + g (\rho \beta_\Theta)_{nf} (\Theta(\zeta, \tau) - \Theta_\infty) + g (\rho \beta_\Phi)_{nf} (\Phi(\zeta, \tau) - \Phi_\infty) \quad (1)$$

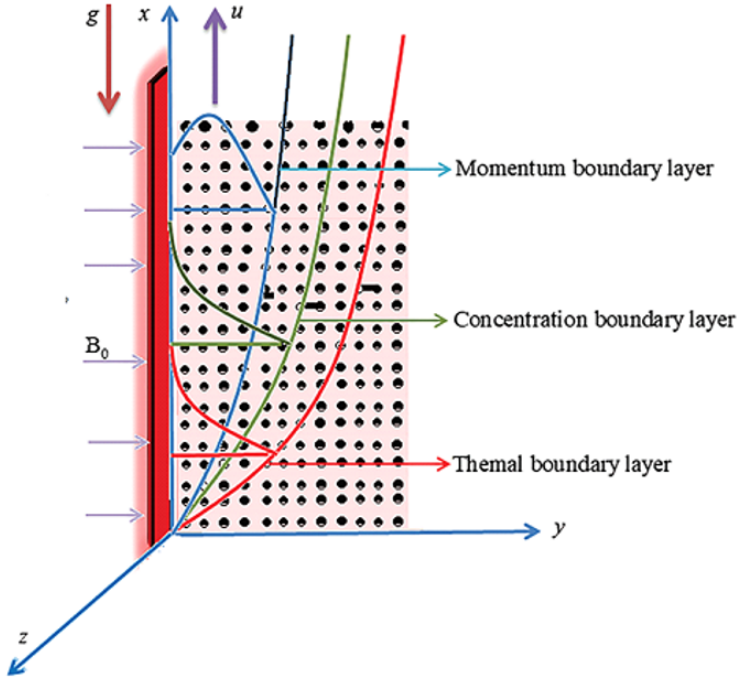


Figure 1. Illustration of the flow regime

The energy equation, which incorporates both heat generation and the influence of thermal radiation, can be expressed as follows:

$$(\rho C_p)_{nf} \frac{\partial \Theta(\zeta, \tau)}{\partial \tau} + Q_0 (\Theta(\zeta, \tau) - \Theta_\infty) = k_{nf} \left(1 + \frac{16\sigma^* \Theta_\infty^3}{3k^* k_{nf}} \right) \frac{\partial^2 T(\zeta, \tau)}{\partial \zeta^2} - \frac{\partial q_r}{\partial \zeta} \quad (2)$$

The presence of a first-order chemical reaction influences the concentration equation, which is articulated as follows:

$$\frac{\partial \Phi(\zeta, \tau)}{\partial \tau} + \kappa_r (\Phi(\zeta, \tau) - \Phi_\infty) = D_{nf} \frac{\partial^2 \Phi(\zeta, \tau)}{\partial \zeta^2} \quad (3)$$

The analysis is further defined by a set of prescribed initial and boundary conditions, described in:

$$\begin{aligned} u(\zeta, \tau) &= 0, \quad \Theta(\zeta, \tau) = \Theta_\infty, \quad \Phi(\zeta, \tau) = \Phi_\infty, \text{ for } \tau = 0, \text{ and } \zeta \geq 0 \\ u(\zeta, \tau) - \eta \frac{\partial u(\zeta, \tau)}{\partial \zeta} &= B\tau^p, \quad \left. \frac{\partial \Theta(\zeta, \tau)}{\partial \zeta} \right|_{\zeta=0} = -h_s \Theta(\zeta, \tau), \quad \Phi = \Phi_p, \text{ for } \zeta = 0, \text{ and } \tau > 0 \\ u(\zeta, \tau) &\rightarrow 0, \quad \Theta(\zeta, \tau) \rightarrow \Theta_\infty, \quad \Phi(\zeta, \tau) = \Phi_\infty. \text{ as } \zeta \rightarrow \infty \text{ and } \tau > 0 \end{aligned} \quad (4)$$

where, ρ_{nf} denotes the density, μ_{nf} represents the dynamic viscosity, σ_{nf} is the electrical conductivity, k_{nf} denotes the thermal conductivity, $(\rho\beta_T)_{nf}$ represents the thermal volumetric expansion, $(\rho\beta_C)_{nf}$ is the mass volumetric expansion, and $(\rho C_p)_{nf}$ denotes the specific heat capacitance of the nanofluid. The mathematical relationship between the nanofluid and the regular fluid is given as follows:

$$\begin{aligned} \mu_{nf} &= \frac{\mu_{Cf}}{(1-\phi)^{2.5}}, \quad \rho_{nf} = (1-\phi)\rho_{Cf} + \phi\rho_c, \quad (\rho C_p)_{nf} = (1-\phi)(\rho C_p)_{Cf} + \phi(\rho C_p)_c \\ (\rho\beta_T)_{nf} &= (1-\phi)(\rho\beta_T)_{Cf} + \phi(\rho\beta_T)_c \cdot (\rho\beta_C)_{nf} = (1-\phi)(\rho\beta_C)_{Cf} + \phi(\rho\beta_C)_c \\ \sigma_{nf} &= \sigma_{Cf} \left[1 + \frac{3 \left(\frac{\sigma_c}{\sigma_{Cf}} - 1 \right) \phi}{\left(\frac{\sigma_c}{\sigma_{Cf}} + 2 \right) - \left(\frac{\sigma_c}{\sigma_{Cf}} - 1 \right) \phi} \right], \quad k_{rf} = k_{Cf} \left[\frac{k_c + 2k_{Cf} - 2\phi(k_{Cf} - k_c)}{k_c + 2k_{Cf} + 2\phi(k_{Cf} - k_c)} \right] \end{aligned} \quad (5)$$

Table 1 presents the thermophysical properties of both the base fluid and the nanoparticles under consideration.

Table 1. Characteristics of the cementitious fluid and clay nanoparticles [9]

	$\rho(\text{kg/m}^3)$	$C_p(\text{J/kgK})$	$K(\text{W/mK})$	$\beta_\Theta \times 10^{-5} (\text{K}^{-1})$
Clay Nanoparticles	6320	531.8	76.5	1.80
Cementitious Fluid	5.61	1.160	41.086	1.57

2.1 Generalization of the Classical Model

This section outlines the procedure for dimensional analysis, which involves converting the classical dimensional model into a dimensionless one. By integrating dimensionless variables, the governing equations were initially transformed into a dimensionless format and then fractionalized by introducing the time fractional derivative operator of the *CPC* derivative.

The following suitable dimensionless quantities make the governing equations dimensionless:

$$v = \frac{u}{\left[v_f^p B\right]^{\frac{1}{2p+1}}}, y = \zeta \left[\frac{B}{v_f^{p+1}} \right]^{\frac{1}{2p+1}}, t = \tau \left[\frac{B^2}{v_f} \right]^{\frac{1}{2p+1}}, T = \frac{\Theta - \Theta_\infty}{\Theta_p - \Theta_\infty}, C = \frac{\Phi - \Phi_\infty}{\Phi_p - \Phi_\infty} \quad (6)$$

Eqs. (1)-(4) can be expressed as follows using Eqs. (5) and (6):

$$\begin{aligned} \frac{\partial v(y, t)}{\partial t} &= \frac{\alpha_0}{1 + \lambda_1} \left(1 + \lambda \frac{\partial}{\partial t} \right) \frac{\partial^2 v(y, t)}{\partial y^2} + \frac{\alpha_1}{1 + \lambda_1} \left(1 + \lambda \frac{\partial}{\partial t} \right) v(y, t) - Mv(y, t) \\ &+ GrT(y, t) + GmC(y, t) \end{aligned} \quad (7)$$

$$\frac{\partial T(y, t)}{\partial t} + \Psi T(y, t) = \frac{a_2}{Pr} \frac{\partial^2 T(y, t)}{\partial y^2} \quad (8)$$

$$\frac{\partial C(y, t)}{\partial t} + \beta C(y, t) = \frac{1}{Sc} \frac{\partial^2 C(y, t)}{\partial y^2} \quad (9)$$

$$\left. \begin{aligned} v(y, t) &= 0, & T(y, t) &= 0, & C(y, t) &= 0; & t = 0 & \text{and} & y \geq 0 \\ v(y, t) - \eta^* \frac{\partial u(y, t)}{\partial y} &= t^p, & \frac{\partial T(y, t)}{\partial y} + \delta[1 + T(y, t)] &= 0, & C(y, t) &= 1; & y = 0 & \text{and} & t > 0, \\ v(y, t) &\rightarrow 0, & T(y, t) &\rightarrow 0, & \Phi(y, t) &\rightarrow 0; & \text{as } y \rightarrow 0. \end{aligned} \right\} \quad (10)$$

The incorporation of the *CPC* operator leads to unitless governing equations in the following forms:

$$\begin{aligned} {}^{CPC}D_t^\gamma v(y, t) &= \frac{\alpha_0}{1 + \lambda_1} \left(1 + \hat{\lambda} {}^{CPC}D_t^\gamma \right) \frac{\partial^2 v(y, t)}{\partial y^2} + \frac{\alpha_1}{1 + \hat{\lambda}_1} \left(1 + \hat{\lambda} {}^{CPC}D_t^\gamma \right) v(y, t) - Mv(y, t) \\ &+ GrT(y, t) + GmC(y, t) \end{aligned} \quad (11)$$

$${}^{CPC}D_t^\gamma T(y, t) + \Psi T(y, t) = \frac{a_2}{Pr} \frac{\partial^2 T(y, t)}{\partial y^2} \quad (12)$$

$${}^{CPC}D_t^\gamma C(y, t) + \beta C(y, t) = \frac{1}{Sc} \frac{\partial^2 C(y, t)}{\partial y^2} \quad (13)$$

where, ${}^{CPC}D_t^\gamma$ is the time-fractional *CPC* operator, which is defined as follows along with its Laplace transformation [18].

$${}^{CPC}D_t^\gamma g(t) = \frac{1}{\Gamma(1 - \gamma)} \int_0^\tau (k_1(\gamma)g(t) + k_0(\gamma)(t)) (t - \tau)^{-\delta} d\tau \quad (14)$$

$$\mathfrak{L}({}^{CPC}D_i^\gamma g(\tau)) = \left[\frac{k_1(\gamma)}{q} + k_0(\gamma) \right] q^\gamma \overline{g(q)} - k_0(\gamma) q^{\gamma-1} g(0) \quad (15)$$

where, q is the inverse Laplace transformed variable of t , and $k_0(\gamma)$ and $k_1(\gamma)$ are the functions of γ .

2.2 Flow Analysis with the CPC Fractional Differential Operator

The integral transform approach, also known as the Laplace transform technique, was utilized to solve the time-fractional governing equation mathematically.

Utilizing the Laplace transform operator along with the prescribed initial conditions in Eqs. (11), (12) and (13), the following equations can be obtained:

$$\begin{aligned} & \frac{\alpha_0}{1 + \lambda_1} \left(1 + \hat{\lambda} q^\gamma \left(\frac{k_1(\gamma)}{q} + k_0(\gamma) \right) \right) \frac{d^2 \bar{v}(y, q)}{dy^2} - q^\gamma \left(\frac{k_1(\gamma)}{q} + k_0(\gamma) \right) \bar{v}(y, q) - M \bar{v}(y, q) \\ & - \frac{\alpha_0}{1 + \lambda_1} \left(1 + \hat{\lambda} q^\gamma \left(\frac{k_1(\gamma)}{q} + k_0(\gamma) \right) \right) \bar{v}(y, q) + Gr^- \bar{v}(y, q) + Gm \bar{v}(y, q) = 0 \end{aligned} \quad (16)$$

$$\frac{a_2}{Pr} \frac{d^2 \bar{T}(y, q)}{dy^2} - \left(\left(\frac{k_1(\gamma)}{q} + k_0(\gamma) \right) q^\gamma + \Psi \right) \bar{T}(y, q) = 0 \quad (17)$$

$$\left(\frac{k_1(\gamma)}{q} + k_0(\gamma) \right) q^\gamma \bar{C}(y, q) - (Sc)^{-1} \frac{d^2 \bar{C}(y, q)}{dy^2} + \beta \bar{C}(y, q) = 0 \quad (18)$$

The Laplace transformed boundary conditions are as follows:

$$\left. \begin{array}{l} \bar{v}(0, q) - \eta^* \frac{d\bar{v}(0, q)}{dy} = \frac{\Gamma(p+1)}{q^{p+1}}, \quad \text{and} \quad \bar{v}(\infty, q) = 0 \\ \frac{\partial \bar{T}(0, q)}{\partial y} + \delta \left[\frac{1}{q} + \bar{T}(0, q) \right] = 0 \quad \text{and} \quad \bar{T}(\infty, q) = 0 \\ \bar{C}(0, q) = \frac{1}{q} \quad \text{and} \quad \bar{C}(\infty, q) = 0 \end{array} \right\} \quad (19)$$

The following equations can be obtained by simplifying Eqs. (17), (18) and (19) and incorporating transformed boundary conditions:

$$\begin{aligned} \bar{v}(y, q) &= \left[\left[\eta + \sqrt{\frac{\Re_2}{\Re_1}} \right] \left[\frac{\Gamma(p+1)}{\eta \cdot q^{p+1}} + \frac{Gr \Re_2 (1 + \sqrt{\Re_3})}{q \sqrt{\Re_4} (\Re_2 \Re_3 - \Re_1)} + \frac{Gm \Re_2 (1 + \sqrt{\Re_5})}{q (\Re_5 \Re_2 - \Re_1)} \right] \right] \exp \left(-y \sqrt{\frac{\Re_1}{\Re_2}} \right) \\ & - \frac{\Re_2 Gr \exp(-y \sqrt{\Re_3})}{q \sqrt{\Re_4} (\Re_3 \Re_2 - \Re_1)} - \frac{\Re_2 Gm \exp(-y \sqrt{\Re_5})}{q (\Re_5 \Re_2 - \Re_1)} \end{aligned} \quad (20)$$

$$\bar{T}(y, q) = \frac{1}{q \sqrt{\frac{Pr}{a_2} \left(\frac{k_1(\gamma)}{q} + k_0(\gamma) \right) q^\gamma + \Psi - \delta}} \exp \left(-y \sqrt{\frac{Pr}{a_2} \left(\frac{k_1(\gamma)}{q} + k_0(\gamma) \right) q^\gamma + \Psi} \right) \quad (21)$$

$$\bar{C}(y, q) = \frac{1}{q} \exp \left(-y \sqrt{Sc \left(\frac{k_1(\gamma)}{q} + k_0(\gamma) \right) q^\gamma + \beta} \right) \quad (22)$$

It is extremely complex to manually look for the inverse Laplace transform solution for Eqs. (20), (21) and (22). Therefore, Zakian's algorithm, a numerical method, was employed.

2.3 Nusselt and Sherwood Number

The rates of heat and mass transfer are given as follows:

$$Nu = - (\text{Re}) \left(\frac{k_{nf}}{k_f} + R_d \right) \frac{\partial T(y, t)}{\partial y} \Big|_{y=0} \quad (23)$$

$$Sh = -D_{nf} \left(\frac{\partial C(y, t)}{\partial y} \right)_{y=0} \quad (24)$$

3 Results and Discussion

This section mainly aims to provide detailed physical arguments for the graphical results of the fluid flow problem. The time variant of electrically conducting Jeffrey nanofluid flow on a vertical flat plate was investigated under the impact of slip conditions and Newtonian heating. The first-order chemical reaction and heat generation were also considered in this study. By including relative dimensionless entities, the controlling equations were made dimensionless, and then fractionalized using the operator of CPC fractional derivative. The Laplace transform technique was used to derive the closed-form solution for the governing equations. The impact of dimensionless physical characteristics on fluid flow, heat, and mass distribution was depicted for graphical examination.

Figure 2 depicts the influence of the fractional order on mass distribution. The fractional model offers a broader perspective compared to ordinary models, particularly concerning fluid layers. Within the fractional model, an infinite number of fluid layers can be represented between 0 and 1, allowing for a more detailed characterization of complex fluid behaviors. This feature is particularly advantageous for experimentalists seeking to compare their work with the most fitting layers within the model. Furthermore, the fractional-order parameter encapsulates the memory effect of the fluid, a characteristic not captured by classical models. The graph in Figure 2 illustrates that mass distribution is indeed an increasing function of the fractional-order parameter, highlighting the significance of considering fractional models in fluid dynamics analyses.

Figure 3 shows the impact of chemical reactions characterized by the parameter β on mass distribution. A decrease in the mass distribution profile can be observed. As the value of β increases, the distribution of mass in the fluid slows down because chemical reactions increase the number of species in the mass, which in turn retards the mass distribution, leading to the observed decrease.

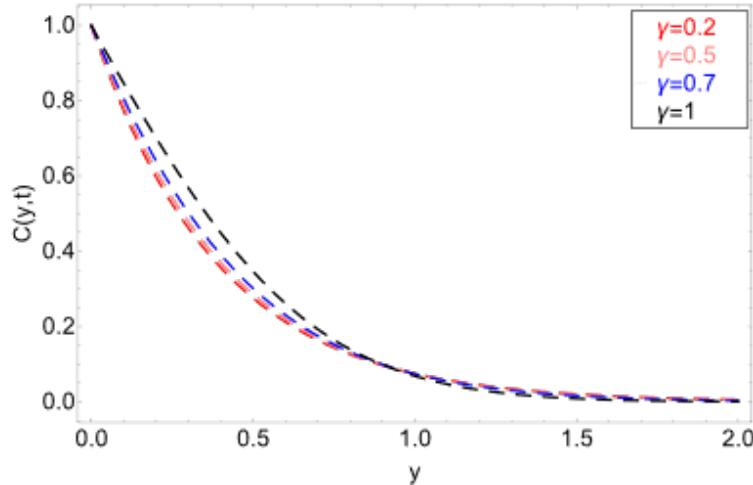


Figure 2. Variation in mass distribution against fractional order γ

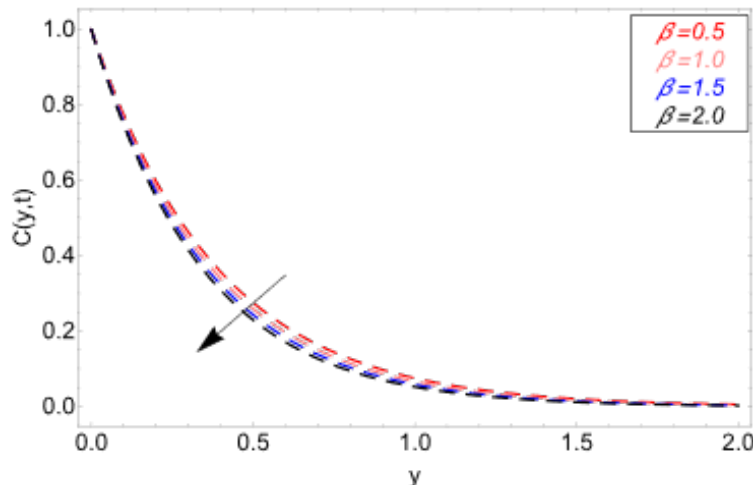


Figure 3. Variation in mass distribution against chemical reaction parameter β

Figure 4 shows the impact of the volume fraction of clay nanoparticles on mass distribution. When the mass distribution decreases, clay nanoparticles increase. Several factors contribute to the decrease in mass distribution that occurs when the volume fraction of clay nanoparticles increases. Clay nanoparticles have a high surface area-to-volume ratio, which means that as their volume fraction increases, there is a greater surface area available for interaction with the surrounding medium. This increased surface area leads to greater agglomeration or clustering of the nanoparticles, effectively reducing their individual mobility within the medium. Consequently, the nanoparticles become more prone to forming larger aggregates or clusters, which impedes their dispersion throughout the medium and results in a decrease in mass distribution. Additionally, the increased presence of clay nanoparticles can alter the rheological properties of the medium, such as viscosity and flow behavior, further contributing to the observed decrease in mass distribution. Therefore, the decrease in mass distribution with increasing volume fractions of clay nanoparticles is primarily attributed to their enhanced tendency to form aggregates, which hinders their uniform dispersion within the medium.

Figure 5 depicts the influence of the Schmidt number (Sc) on mass distribution. A decline in the mass distribution profile can be observed. When the Schmidt number increases, it indicates that momentum diffusivity becomes relatively more dominant compared to mass diffusivity. This shift in dominance implies an increase in the fluid's efficiency in transporting momentum (i.e., an increase in the rate of momentum transfer within the fluid), but a decrease in its efficiency in transporting mass (i.e., a decrease in the rate of mass transfer within the fluid). As a result, the dispersion or spreading of mass within the fluid becomes less pronounced, leading to a decrease in mass distribution. Essentially, as the Schmidt number increases, the fluid becomes more effective at transferring momentum than mass, which hampers the dispersion of particles or substances within the fluid, resulting in a decrease in mass distribution.

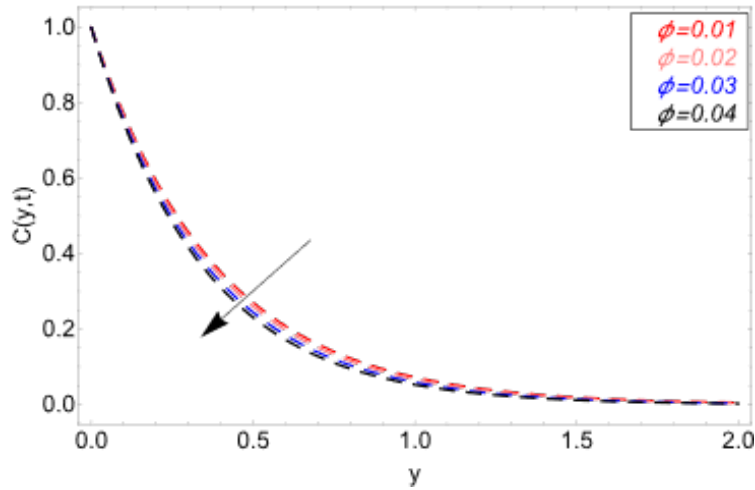


Figure 4. Variation in mass distribution against the volume fraction ϕ

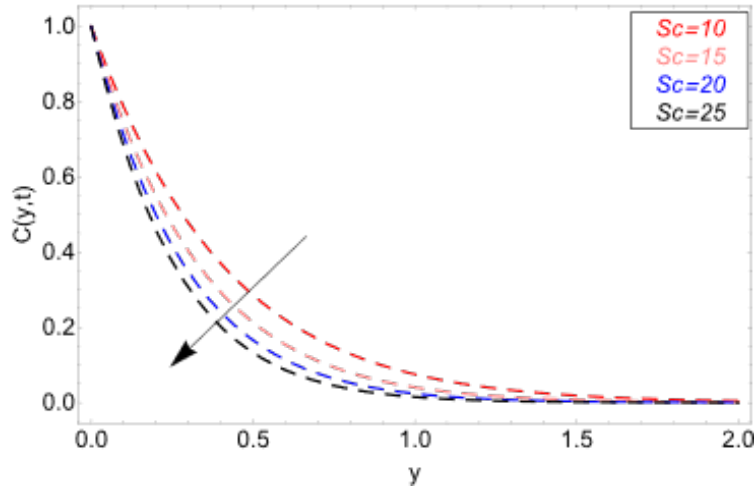


Figure 5. Variation in mass distribution against the Schmidt number Sc

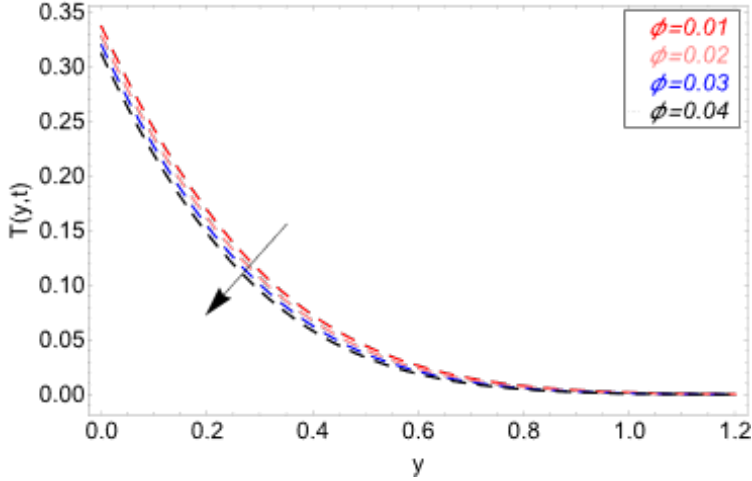


Figure 6. Variation in temperature distribution against the volume fraction ϕ

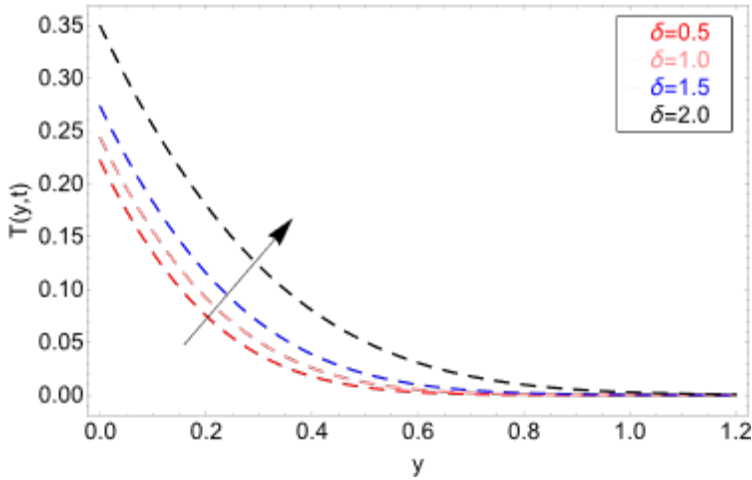


Figure 7. Variation in temperature distribution against the Newtonian heating parameter δ

Figure 6 shows the impact of volume fraction on the thermal field. The thermal field profile decreases as the magnitude of the volume fraction increases. Clay nanoparticles possess unique thermal properties, including a high specific surface area and thermal conductivity. When dispersed within a medium, such as a fluid or a polymer matrix, these nanoparticles can alter the heat transfer characteristics of the system. As the volume fraction of clay nanoparticles increases, so does the interfacial area between the nanoparticles and the surrounding medium. This greater interfacial area enhances the interactions between the nanoparticles and the medium, leading to more effective heat conduction pathways. Consequently, heat transfer within the system becomes more efficient, resulting in a decrease in temperature.

Figure 7 depicts the behavior of the thermal field in response to the Newtonian heating parameter δ . An increase in the thermal field can be observed for larger values of the Newtonian heating parameter δ . The observed increase in temperature profile with an increase in the Newtonian heating parameter can be attributed to the fundamental principles of heat transfer. The Newtonian heating parameter quantifies the intensity of heat generation within a system per unit volume, typically through external sources such as joule heating or other forms of applied heating. As the Newtonian heating parameter increases, it signifies a higher rate of heat generation within the system. This increased heat input leads to a rise in the temperature gradient within the medium as more energy is supplied to the system. As a result, the system's temperature rises to handle the extra heat production.

Figure 8 presents the influence of the radiation parameter on the thermal distribution profile. It can be observed that the thermal field increases when the value of the radiation parameter increases. When the radiation parameter increases, it indicates that radiative heat transfer becomes more dominant in the overall heat transfer process. Radiative heat transfer involves the emission, absorption, and scattering of electromagnetic radiation within a medium. As the radiation parameter increases, the rate of energy transfer via radiation intensifies, leading to a greater influx of energy into the system. This additional energy absorption results in an elevation of the temperature profile throughout

the medium. Moreover, radiative heat transfer is particularly effective in transferring energy across large distances and through optically transparent media. Therefore, as the radiation parameter increases, the influence of radiative heat transfer becomes more pronounced, leading to a more significant increase in the temperature profile within the system.

Figure 9 illustrates the impact of the heat absorption coefficient Ψ on the thermal field of the clay-based nanofluid. The heat absorption coefficient represents the ability of a material to absorb thermal energy from its surroundings. When the heat absorption coefficient increases, it implies that the material becomes more effective at absorbing heat energy. Consequently, the material absorbs more heat energy, resulting in a decrease in the thermal energy available for heating the surrounding environment. This decrease in available thermal energy results in a lower temperature profile within the system. Furthermore, the material's increased absorption of heat energy can reduce the heat transfer to nearby regions or materials, thereby exacerbating the overall temperature profile decrease.

Figure 10 illustrates the behavior of the velocity field against the slip condition parameter η . A decline in the field of velocity for larger values of η can be observed. As the magnitude of the slip condition parameter increases, the frictional resistance between the fluid particles and the boundaries also increases. This heightened friction impedes fluid motion, resulting in a decline in the velocity profile.

Figure 11 shows the variation in the velocity field concerning the thermal Grashof number (Gr). The velocity field is an increasing function of Gr . The increase in velocity profile with an increase in the thermal Grashof number can be attributed to buoyancy-driven flow effects. The thermal Grashof number quantifies the ratio of buoyancy to viscous forces in a fluid flow due to temperature differences. As the thermal Grashof number increases, the buoyancy force becomes more dominant compared to viscous forces. This dominance of buoyancy causes stronger fluid motion and improves convective heat transfer. Consequently, the velocity profile increases as the thermal Grashof number increases due to the intensified buoyancy-driven flow within the fluid.

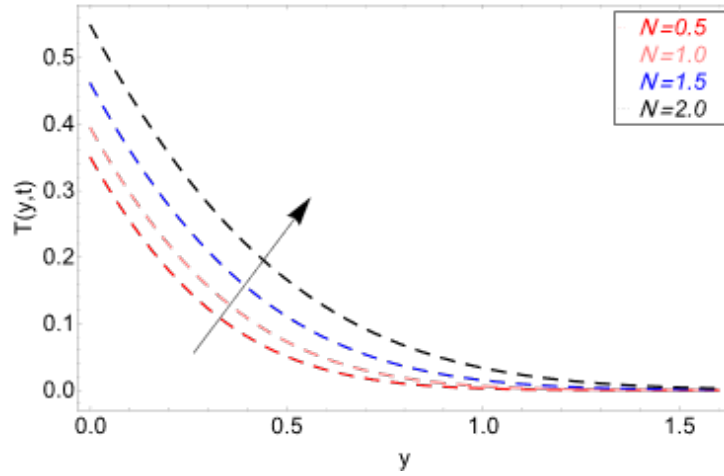


Figure 8. Variation in temperature distribution against the radiation parameter N

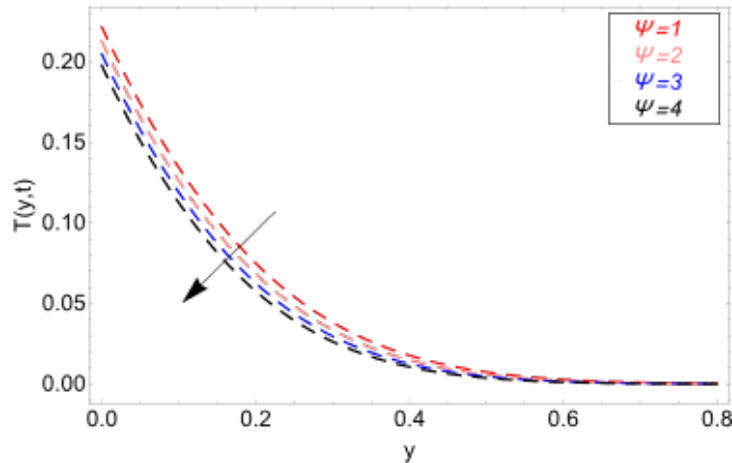


Figure 9. Variation in temperature distribution against the heat absorption coefficient Ψ

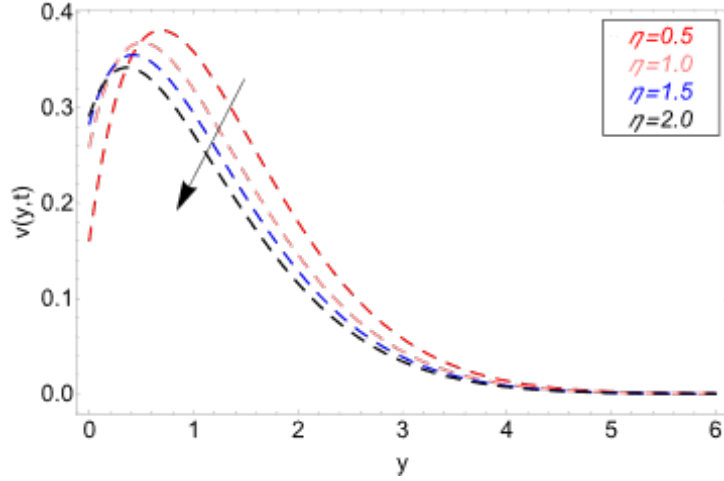


Figure 10. Variation in velocity profile against the slippage condition parameter η

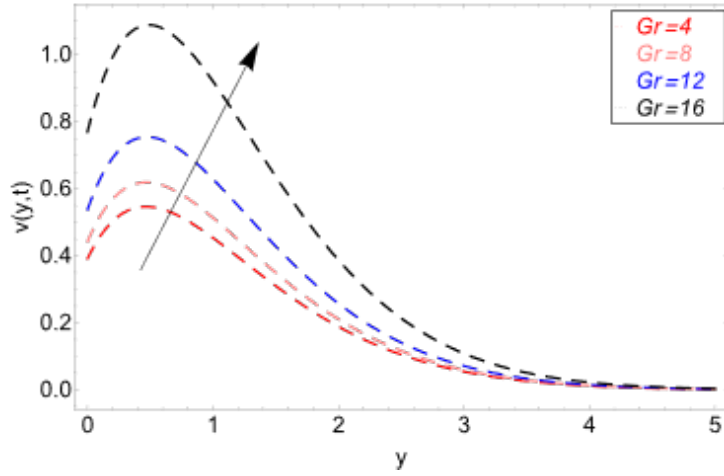


Figure 11. Variation in velocity profile against the thermal Grashof number Gr

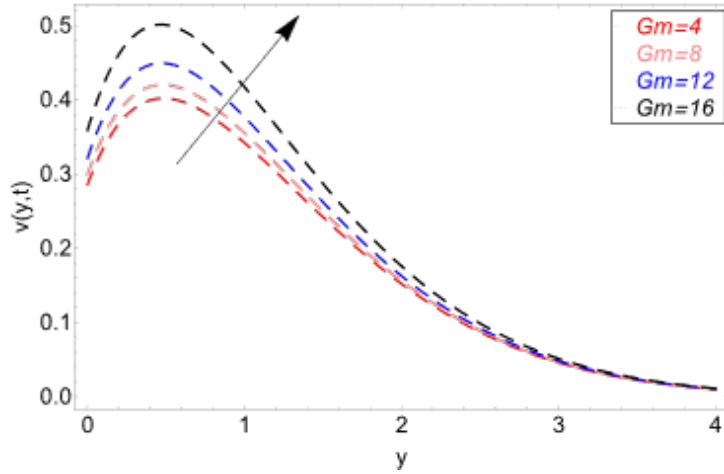


Figure 12. Variation in velocity profile against the mass Grashof number Gm

The variation in the velocity profile against the mass Grashof number Gm is depicted in Figure 12. An increase in the profile can be observed for a greater magnitude of Gm . The increase in velocity profile with an increase in the Gm can be attributed to buoyancy-driven flow effects similar to those seen in thermal Grashof numbers. The Gm quantifies the ratio of buoyancy to viscous forces in a fluid flow due to concentration differences. As Gm increases,

buoyancy becomes more dominant relative to viscous forces. This dominance of buoyancy induces stronger fluid motion, leading to an increase in velocity profile as the mass Grashof number increases.

Figure 13 displays the conclusion of the time relaxation parameter λ on the velocity profile. In response to higher values of the time relaxation parameter, a rise in the velocity profile can be observed. When the parameter value increases, the fluid motion accelerates due to the quick response of the shear stress. Figure 14 shows the influence of the time retardation parameter λ_1 on the profile of velocity. As the parameter's value increases, the shear stress experiences a delay response, slowing down the fluid motion, leading to a drop in the velocity profile due to its greater magnitude.

Figure 15 illustrates the effect of the magnetic parameter M . A decreasing trend can be observed in the figure. When the magnetic parameter increases, the strength of the applied magnetic field becomes more significant. This stronger magnetic field exerts greater forces on the fluid, leading to enhanced fluid motion through mechanisms such as magnetohydrodynamic (MHD) effects. These effects include the Lorentz force, which acts perpendicular to both the magnetic field and the direction of fluid flow, resulting in increased fluid velocities. Consequently, as the magnetic parameter increases, the impact of the magnetic field on the fluid becomes more pronounced, leading to higher velocities in the velocity profile.

While Figure 16 shows the influence of the permeability parameter K . An opposite trend compared to the magnetic parameter can be observed in the figure. The increased porosity creates enhanced flow pathways, leading to an increase in the velocity profile. When the porosity parameter increases, it signifies a higher proportion of void spaces within the medium, allowing more fluid to pass through. These additional flow pathways reduce flow resistance, enabling the fluid to move more freely through the porous medium. Consequently, as the porosity parameter increases, the overall velocity profile rises, indicating the enhanced fluid mobility made possible by the increased porosity.

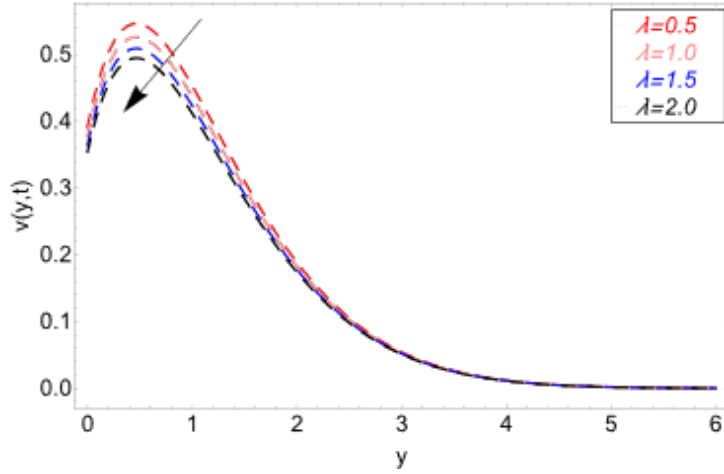


Figure 13. Variation in velocity profile against the time relaxation parameter λ

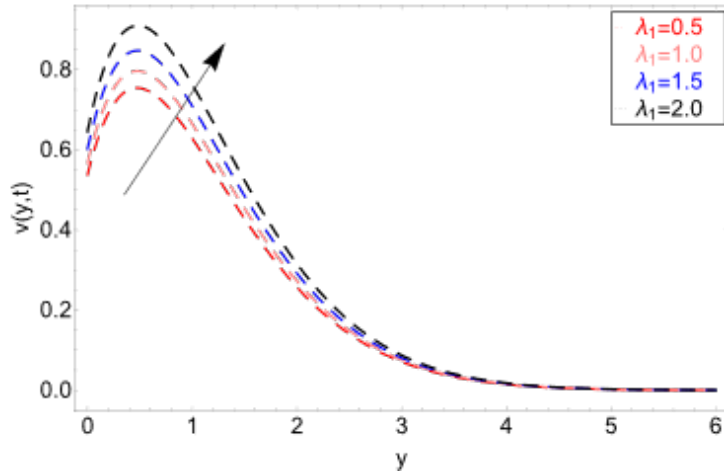


Figure 14. Variation in velocity profile against the time retardation parameter λ_1

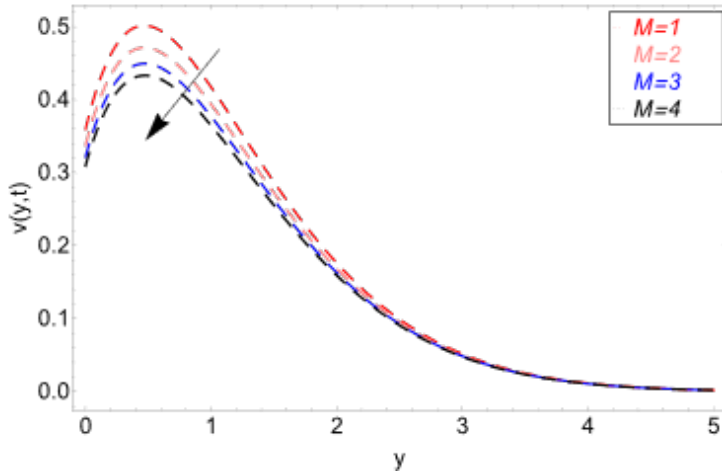


Figure 15. Variation in velocity profile against the magnetic parameter M

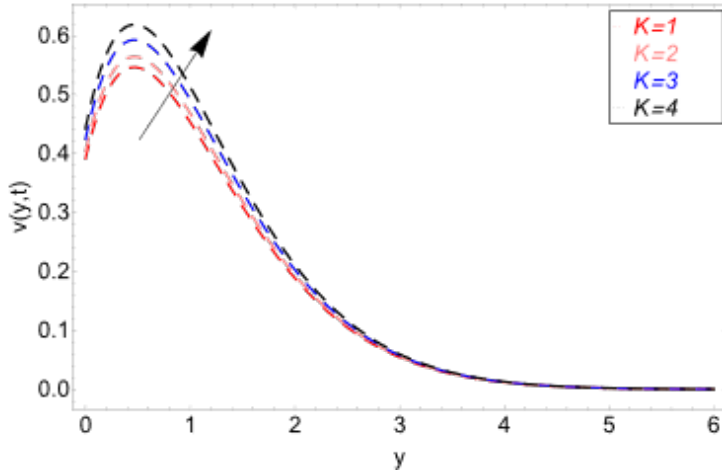


Figure 16. Variation in velocity profile against the permeability parameter K

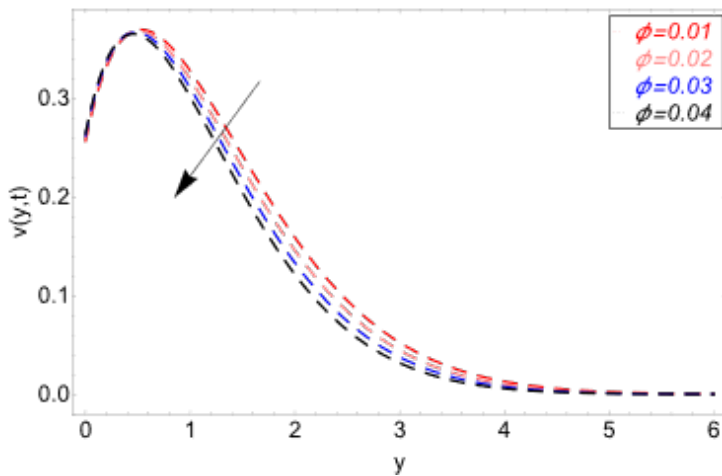


Figure 17. Variation in velocity profile against the volume fraction ϕ

Figure 17 illustrates the influence of the clay nanoparticle volume fraction ϕ on fluid velocity. Increased values of the volume fraction result in a decrease in fluid motion. As the volume fraction of clay nanoparticles increases, more nanoparticles are dispersed within the fluid, leading to greater interactions between particles and the fluid molecules. This results in an increase in the effective viscosity of the fluid-nanoparticle mixture, impeding fluid

flow. Additionally, nanoparticles disrupt the fluid's laminar flow, causing turbulence and further slowing down fluid velocity. Consequently, as the volume fraction of clay nanoparticles increases, the velocity profile decreases due to increased viscosity and disrupted flow dynamics within the fluid.

Figure 18 presents a comparative analysis between this study and previously published research. The solution proposed in this study was validated against the findings of Ahmad et al. [19] by setting $\lambda, \lambda_1 \rightarrow 0$.

Table 2 and Table 3 examine the rates of mass and heat transfer in the fluid influenced by clay nanoparticles. Table 2 reveals that the fluid containing clay particles exhibits a higher transfer rate compared to conventional fluids. As the volume fraction of clay particles gradually increases, the rate of heat transfer decreases by 10.17%. This reduction is important for engineers in the cooling and energy-saving sectors. Table 3 shows the mass transfer rate of the nanofluid with respect to clay nanoparticles. The mass transfer rate decreases by 1.31% as the volume fraction of clay nanoparticles reaches 0.04. This decrease is beneficial for enhancing the bonding force, tensile strength, and heat resistibility of the cementitious fluid.

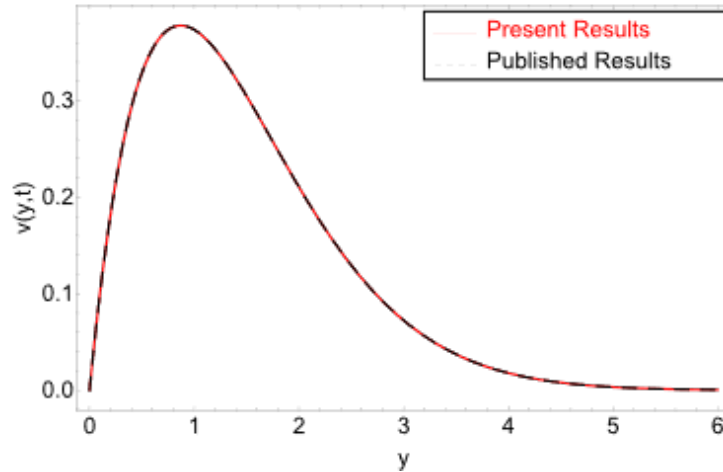


Figure 18. Comparative analysis of the suggested solution with the solution proposed by Ahmad et al. [19]

Table 2. Variation in the Sherwood number against ϕ

ϕ	S_h	Decrease in Mass Distribution
0.00	2.286	–
0.01	2.279	0.31%
0.02	2.271	0.66%
0.03	2.265	0.92%
0.04	2.256	1.31%

Table 3. Variation in the Nusselt number against ϕ

ϕ	N_u	Decrease in Heat Transfer
0.00	1.563	–
0.01	1.529	2.17%
0.02	1.493	4.48%
0.03	1.443	7.68%
0.04	1.404	10.17%

4 Conclusion

Jeffrey nanofluid was analyzed in response to heat generation and chemical reactions on a vertical flat plate. A homogenous mixture of clay nanoparticles formed nano-cementitious fluids. The effect of Newtonian heating and slip was considered under physical conditions. The mathematical governing equation was formulated in terms of partial differential equations and then fractionalized with the CPC operator. The closed-form solutions for velocity, thermal, and concentration fields were obtained by applying the Laplace transform technique. The key results which can be observed during the analysis are as follows:

(1) The concentration field is inversely proportional to both chemical reactions and the Schmidt number, whereas it increases with the fractional order and volume fraction of clay nanoparticles.

(2) The thermal field exhibits an increase with a higher fractional order, the presence of radiation, and the Newtonian heating parameter, while it decreases as the heat absorption coefficient and nanoparticle volume fraction increase.

(3) The velocity profile is positively affected by the fractional order, thermal and mass Grashof numbers, and the permeability parameter. However, it shows a decrease with increased magnetic parameters and nanoparticle volume fraction.

(4) The presence of clay nanoparticles, when reaching a volume fraction of 0.04, leads to a reduction in both the heat transfer rate by 10.17% and the mass transfer rate by 1.31%.

Author Contributions

Saqib Murtaza and Zubair Ahmad prepared the manuscript with equal contributions.

Data Availability

The data supporting the findings of this study are available from the corresponding author upon reasonable request.

Conflicts of Interest

The authors declare that they have no conflict of interest.

References

- [1] L. Laim, H. Caetano, and A. Santiago, “Effects of nanoparticles in cementitious construction materials at ambient and high temperatures,” *J. Bldg. Eng.*, vol. 35, no. 1, pp. 1–14, 2021. <https://doi.org/10.1016/j.jobe.2020.102008>
- [2] Y. He, L. Lu, K. Sun, F. Wang, and S. Hu, “Electromagnetic wave absorbing cement-based composite using Nano-Fe₃O₄ magnetic fluid as absorber,” *Cem. Concr. Compos.*, vol. 92, no. 1, pp. 1–6, 2018. <https://doi.org/10.1016/j.cemconcomp.2018.05.004>
- [3] J. Jiang, S. C. Kong, J. H. Zhu, and C. Pei, “Enhancing and functionalizing cement mortar with one-step water-based graphene nanofluid additives,” *Constr. Build. Mater.*, vol. 4, no. 16, pp. 1–16, 2024. <https://doi.org/10.1016/j.conbuildmat.2024.135104>
- [4] A. Nasiri, A. Rashidi, M. Shariaty-Niasar, and H. Soltanian, “Preparation and application of carbon nanotube nanofluid as a reinforcement of cement slurry,” *Adv. Cem. Res.*, vol. 26, no. 3, pp. 177–184, 2014. <https://doi.org/10.1680/adcr.13.00007>
- [5] M. A. Khan, M. K. Imam, K. Irshad, H. M. Ali, M. A. Hasan, and S. Islam, “Comparative overview of the performance of cementitious and non-cementitious nanomaterials in mortar at normal and elevated temperatures,” *Nanomaterials*, vol. 11, no. 4, pp. 1–30, 2021. <https://doi.org/10.3390/nano11040911>
- [6] A. A. A. Hadi, “Nanoparticles concentration and environmental effects on cogeneration system in cement industry,” *Int. J. Eng. Res. Gen. Sci.*, vol. 3, no. 1, pp. 786–798, 2015. <https://doi.org/10.3390/nano11040911>
- [7] P. Zhang, S. Han, G. L. Golewski, and X. Wang, “Nanoparticle-reinforced building materials with applications in civil engineering,” *Adv. Mech. Eng.*, vol. 12, no. 10, pp. 1–4, 2020. <https://doi.org/10.1177/1687814020965438>
- [8] N. A. Sheikh, D. L. Chuan Ching, I. Khan, A. Ahmad, and S. Ammad, “Concrete based jeffrey nanofluid containing zinc oxide nanostructures: Application in cement industry,” *Symmetry*, vol. 12, no. 6, pp. 1–17, 2020. <https://doi.org/10.3390/sym12061037>
- [9] S. Murtaza, M. Iftekhar, F. Ali, and I. Khan, “Exact analysis of non-linear electro-osmotic flow of generalized maxwell nanofluid: Applications in concrete based nano-materials,” *IEEE Access*, vol. 8, no. 1, pp. 96 738–96 747, 2020. <https://doi.org/10.1109/ACCESS.2020.2988259>
- [10] D. Khan, P. Kumam, I. Khan, A. Khan, W. Watthayu, and M. Arif, “Scientific investigation of a fractional model based on hybrid nanofluids with heat generation and porous medium: Applications in the drilling process,” *Sci. Rep.*, vol. 12, no. 1, pp. 1–13, 2022. <https://doi.org/10.1038/s41598-022-10398-3>
- [11] S. Murtaza, Z. Ahmad, M. D. Albalwi, Z. Akhtar, M. A. Khan, H. Ahmad, and D. Baleanu, “Caputo time fractional model based on generalized Fourier’s and Fick’s laws for Brinkman-type fluid: Exact solution via integral transform,” *Fractals*, vol. 31, no. 10, pp. 1–14, 2023. <https://doi.org/10.1142/S0218348X23401631>
- [12] Z. Ahmad, S. Crisci, S. Murtaza, and G. Toraldo, “Numerical insights of fractal-fractional modeling of magnetohydrodynamic Casson hybrid nanofluid with heat transfer enhancement,” *Math. Meth. Appl. Sci.*, vol. 2024, no. 1, pp. 1–21, 2024. <https://doi.org/10.1002/mma.10059>

- [13] K. F. Li, C. Q. Yang, Y. B. Zhao, Y. Pan, G. Wang, Y. Y. Zheng, and F. Xu, “Study on the creep behavior of PVA-ECC based on fractional-differential rheological model,” *Constr. Build. Mater.*, vol. 230, no. 1, pp. 1–9, 2020. <https://doi.org/10.1016/j.conbuildmat.2019.117064>
- [14] F. Ali, S. Murtaza, N. A. Sheikh, and I. Khan, “Heat transfer analysis of generalized Jeffery nanofluid in a rotating frame: Atangana–Balaenu and Caputo–Fabrizio fractional models,” *Chaos Solitons Fract.*, vol. 1, no. 29, pp. 1–15, 2019. <https://doi.org/10.1016/j.chaos.2019.08.013>
- [15] M. Gohar, F. Ali, I. Khan, N. A. Sheikh, and A. Shah, “The unsteady flow of generalized hybrid nanofluids: Applications in cementitious materials,” *J. Aust. Ceram. Soc.*, vol. 55, no. 1, pp. 657–666, 2019. <https://doi.org/10.1007/s41779-018-0275-3>
- [16] C. Zhang, Z. Zhu, S. Zhu, Z. He, D. Zhu, J. Liu, and S. Meng, “Nonlinear creep damage constitutive model of concrete based on fractional calculus theory,” *Materials*, vol. 12, no. 9, pp. 1–14, 2019. <https://doi.org/10.3390/ma12091505>
- [17] G. Failla and M. Zingales, “Advanced materials modelling via fractional calculus: Challenges and perspectives,” *Philos. Trans. R. Soc. A*, vol. 378, no. 2172, pp. 1–13, 2020. <https://doi.org/10.1098/rsta.2020.0050>
- [18] D. Baleanu, A. Fernandez, and A. Akgül, “On a fractional operator combining proportional and classical differintegrals,” *Mathematics*, vol. 8, no. 3, pp. 1–13, 2020. <https://doi.org/10.3390/math8030360>
- [19] M. Ahmad, M. I. Asjad, and J. Singh, “Application of novel fractional derivative to heat and mass transfer analysis for the slippage flow of viscous fluid with single-wall carbon nanotube subject to Newtonian heating,” *Math. Meth. Appl. Sci.*, vol. 2021, no. 1, pp. 1–16, 2021. <https://doi.org/10.1002/mma.7332>

Appendix

The constants and dimensionless physical quantities resulting from the calculations are as follow:

$$\begin{aligned}
M &= \frac{\sigma_f B_0^2 b_2}{\rho_f b_0} \left[\frac{v^{1-p}}{B^2} \right]^{\frac{1}{2p+1}}, \quad \frac{1}{K} = \frac{\mu_f \Phi^*}{\rho_f k_1} \left[\frac{v_f}{B^3} \right]^{\frac{1}{2p+1}}, \quad N = \frac{16\sigma^* T_a^3}{3k^* k_f}, \quad \Psi = \frac{Q_0 \left[\frac{v_f}{B^2} \right]^{\frac{1}{2p+1}}}{(\rho C_p)_f a_0}, \\
Gm &= \frac{g (\beta_C)_f b_4 (C_p - C_a) \left[\frac{v_f^{1-p}}{B^3} \right]^{\frac{1}{2p+1}}}{b_0}, \quad Gr = \frac{g (\beta_T)_f b_3 (T_p - T_a) \left[\frac{v^{1-p}}{B^3} \right]^{\frac{1}{2p+1}}}{b_0}, \quad Pr = \frac{\mu_f (C_p)_f}{k_f}, \\
\beta &= \kappa_r \left[\frac{v_f}{B^2} \right]^{\frac{1}{2p+1}}, \quad Sc = \frac{v_f}{D}, \quad b_0 = \left[(1 - \phi) + \phi \frac{\rho_s}{\rho_f} \right], \quad a_1 = \left[\frac{k_s + 2k_f - 2\phi(k_f - k_s)}{k_s + 2k_f + 2\phi(k_f - k_s)} \right], \\
a_2 &= \frac{a_1}{a_0}, \quad b_1 = (1 - \phi)^{-2.5}, \quad b_2 = \left[1 + \frac{3 \left(\frac{\sigma_s}{\sigma_f} - 1 \right) \phi}{\left(\frac{\sigma_s}{\sigma_f} + 2 \right) - \left(\frac{\sigma_s}{\sigma_f} - 1 \right) \phi} \right], \quad b_3 = \left[(1 - \phi) + \phi \frac{(\beta_T)_s}{(\beta_T)_f} \right], \\
\delta &= h_s \left[\frac{v_f^{p+1}}{B} \right]^{\frac{1}{2p+1}}, \quad b_4 = \left[(1 - \phi) + \phi \frac{(\beta_c)_s}{(\beta_c)_f} \right], \quad \alpha = \frac{b_2}{b_0}, \quad \alpha_1 = \frac{\alpha}{K}, \quad \eta^* = \eta \left[\frac{B}{v_f^{p+1}} \right]^{\frac{1}{2p+1}}. \\
\Re_1 &= d_2 + d_3 \chi(\gamma, q), \quad \Re_2 = d_0(1 + \lambda \chi(\gamma, q)), \quad \Re_3 = (a_2)^{-1} \Pr \chi(\gamma, q) + \Psi \\
\Re_4 &= (a_2)^{-1} \Pr \chi(\gamma, q) + \Psi - \delta, \quad \Re_5 = Sc \chi(\gamma, q) + \beta, \quad \chi(\gamma, q) = q^\gamma \left(\frac{k_1(\gamma)}{q} + k_2(\gamma) \right), \\
d_0 &= \frac{\alpha_0}{1 + \lambda_1}, \quad d_1 = M - d_0, \quad d_2 = d_1 - M, \quad d_3 = 1 - d_1
\end{aligned}$$

where, M is the magnetic parameter, K represents the porosity parameter, Gr denotes the thermal Grashof number, Gm is the mass Grashof number, Ψ is the heat generation, Pr represents the Prandtl number, β denotes the chemical reaction parameter, and Sc is the Schmidt number, and $a_1, a_2, b_0, b_1, b_2, b_3, b_4, \alpha$ and α_1 are constants.